Journal of The Electrochemical Society

OPEN ACCESS

A Platinum Micro-Reference Electrode for Impedance Measurements in a PEM Water Electrolysis Cell

To cite this article: Alexandra Hartig-Weiß *et al* 2021 *J. Electrochem. Soc.* **168** 114511

Journal of The Electrochemical Society, 2021 **168** 114511

A Platinum Micro-Reference Electrode for Impedance Measurements in a PEM Water Electrolysis Cell

Alexandra Hartig-Weiß,[1,z] Maximilian Bernt,[1,2] Armin Siebel,[1] and Hubert A. Gasteiger[1,*]

[1]*Chair of Technical Electrochemistry, Department of Chemistry and Catalysis Research Center, Technical University of Munich, 85748 Garching, Germany*
[2]*Bayerisches Zentrum für angewandte Energieforschung, 85748 Garching, Germany*

We present a platinum wire micro-reference electrode (Pt-WRE) suitable for recording individual electrochemical impedance spectra of both the anode and the cathode in a proton exchange membrane water electrolyzer (PEM-WE). For this purpose, a thin, insulated Pt-wire reference electrode (Pt-WRE) was laminated centrally between two 50 μm Nafion® membranes, whereby the potential of the Pt-WRE is determined by the ratio of the local H_2 and O_2 permeation fluxes at the tip of the Pt-WRE. Impedance analysis with the Pt-WRE allows determination of the proton sheet resistance of the anode, the anode catalyst layer capacitance, and the high-frequency resistance (HFR) of both electrodes individually, using a simple transmission-line model. This new diagnostic tool was used to analyze performance degradation during an accelerated stress test (AST), where low and high current densities were alternated with idle periods without current (i.e., at open circuit voltage (OCV)), mimicking the fluctuating operation of a PEM-WE with renewable energy. Our analysis revealed that the increasing HFR that was observed over the course of the OCV-AST, which is the main cause for the observed performance decrease, can unequivocally be assigned to an increasing contact resistance between the anode electrode and the porous transport layer.
 [DOI: 10.1149/1945-7111/ac3717]

Manuscript submitted August 31, 2021; revised manuscript received October 17, 2021. Published November 18, 2021.

In light of an increasing energy demand and the goal to drastically reduce CO_2 emissions, alternative energy carriers produced by renewable energies are a necessity to replace fossil fuels. However, since renewable energies such as wind and solar are inherently intermittent in their power output, an efficient energy carrier provided by a system capable of tolerating such a fluctuating operation is required. Gaseous hydrogen produced by electrochemical spitting of water in a proton exchange membrane water electrolyzer (PEM-WE) is one of the promising technologies that can meet all these requirements.[1,2] Even though PEM-WE durability over 50.000–100.000 h has been demonstrated for constant operation,[3] their durability when operated with renewable energy sources, where times of operation alternate with idle periods where no current is supplied,[4,5] is of greater relevance.

In a previous study by our group, an accelerated stress test (AST) was proposed, with repetitive cycles that consisted of periods of low and high current densities (0.1 Acm^{-2}_{geo} and 3 Acm^{-2}_{geo}), mimicking times of operation, and of an idle period, where the cell was left at open circuit voltage (OCV); this OCV-AST was conducted at 80 °C, with 10 bar pressure on the hydrogen compartment and 1 bar pressure on the oxygen compartment, mimicking the differential pressure operation that would be used in applications where high pressure H_2 is the desired product.[6] Over the course of such an OCV-AST, the performance at 3 Acm^{-2}_{geo} decreased significantly (≈100 mV after 718 cycles), which was attributed to a substantial increase of the high-frequency resistance (HFR) by ≈30 $m\Omega cm^2$ over the 718 cycles. In contrast to that, the HFR remained constant when the cell was polarized at 1.3 V during the idle periods (requiring the supply of only ≈1 $mAcm^{-2}_{geo}$, corresponding to <0.1% of the power at 3 Acm^{-2}_{geo}[6]), proving that the performance degradation is related to the OCV period where the electrolyzer cell voltage drops to near 0 V. By excluding other possible causes for the observed performance degradation, we attributed the increasing HFR to the build-up of a contact resistance at the interface between the anode catalyst layer and the titanium-based porous transport layer (PTL), due to the gradual passivation of the titanium PTL in combination with a decrease of the electronic conductivity of the anode catalyst layer.[6] The latter is triggered by the OCV periods, during which the cell potential drops to ≈0 V due to crossover and accumulation of hydrogen in the anode electrode, thereby gradually reducing the initially crystalline IrO_2 phase of the anode catalyst and forming a hydrous iridium-oxide, which exhibits a lower electronic conductivity.[6,7] While all the observations made in our previous study support our hypothesis of a resistance at the anode||PTL interface being the cause for the observed performance decrease, this could not be proven unambiguously. Therefore, in the present study the processes occurring during the above described OCV-AST are reexamined using a membrane electrode assembly (MEA) into which a micro-reference electrode is incorporated, thereby allowing to record individual electrochemical impedance spectra of anode and cathode with which the origin of different voltage loss contributions can be identified.

Electrochemical impedance spectroscopy (EIS) is a powerful tool to characterize and quantify single performance losses, and there are several examples of reference electrodes being used to study electrochemical cells in the literature.[8,9] Depending on the design of the reference electrode, it can be used to track the half-cell potentials and/or to measure impedance of the individual half-cells. One prominent example often used in the literature to measure half-cell potentials in PEM fuel cells is the dynamic hydrogen electrode (DHE), where usually two thin Pt-wires are placed in close proximity to the active electrode area; by applying a small electrolysis current between the two wires, the potential of the wire where H_2 is being evolved is very close to the reversible hydrogen electrode potential (RHE) due to the fast kinetics for the hydrogen evolution reaction (HER) and can thus be used as a DHE reference electrode (i.e., 0 V vs DHE is only a few mV negative of 0 V vs RHE).[10,11] However, a proper positioning of the DHE reference electrode wire with respect to its distance from the active area of the working and counter electrodes is critical to avoid any potential shift that is caused by the non-linear potential profile in close proximity to the working and counter electrode areas.[12,13] A homogenous potential profile is established at a distance from the edge of the working/counter electrode that is larger than roughly three times the thickness of the ion conducting membrane.[13] Hence, the reference electrode should be placed at the appropriate distance (>3-times the thickness of the ion conducting membrane) from the active electrodes.

*Electrochemical Society Fellow.
[z]E-mail: alexandra.weiss@tum.de

Moreover, a precise geometrical alignment of the working and counter electrode with respect to each other is essential, when seeking to record individual electrode impedance spectra. Adler et al. showed that even a small misalignment (e.g., if the working electrode is protruding beyond the adjacent counter electrode, or vice versa) can lead to erroneous half-cell impedance spectra when acquired with a reference electrode that is placed outside the working/counter electrode area; in this case, the magnitude of the individual electrode impedances are off by a factor of more than two if the counter and working electrodes are misaligned by more than the thickness of the membrane.[12] In summary, with a precise positioning of the DHE reference electrode, the DHE is a suitable tool to monitor half-cell potentials in electrochemical cells like PEM fuel cells or PEM-WEs, but individual electrode impedance spectra should be treated with caution, since a misalignment between the working and counter electrode that is much less than the thickness of the membrane (e.g., 50 μm for a Nafion® 212 membrane) cannot be achieved during fabrication.

In a recently published study, Sorsa et al. used a carbon supported platinum catalyst to coat a ring-shaped Pt electrode on one side of a ≈125 μm thick membrane while a disk-shaped electrolyzer electrode was coated on the other side such that the outer diameter of the disk electrode was smaller than the inner diameter of the concentrically placed ring electrode.[9] Laminating two such membranes together, with the ring electrodes facing each other and with a Pt wire place in between, the Pt ring electrode could be used as pseudo reference electrode.[9] While also here the same artefacts due to the misalignment should occur, the authors used this method to measure the individual impedance contributions. They showed that the anode impedance spectra comprise two main processes, namely mass transport and charge transfer resistances. The interpretation of the cathode spectra, however, turned out to be more complicated due to the occurrence of an inductive loop at low frequencies. Ultimately, the authors concluded that the inductive loop is caused by carbon corrosion of the cathode catalyst layer. This, however, seems highly improbable, as the carbon support is known to be very stable at the potential of an electrolyzer cathode (i.e., at ≈0 V vs RHE), and it should be considered that the cathode impedance spectra could be flawed to electrode misalignment effects (based on the above discussion, misalignment on the order of 250 μm would be expected to lead to such issues).

The artefacts due to a working/counter electrode misalignment can be avoided by placing the reference electrode within the active area of the electrodes. Such an approach was used by Brightman et al., where an external salt bridge containing a hydrogen reference electrode was used to record half-cell potentials during the operation of a PEM water electrolyzer.[14] In their approach, a Nafion® tube enclosed in a PTFE tube was inserted via a hole in the cathode diffusion media and brought in contact with the cathode catalyst layer of the MEA. While this allowed them to show that during electrolyzer operation the main contribution to the overpotential arises from the anode electrode (as expected due to the sluggish kinetics of the oxygen evolution reaction (OER) compared to the HER[15]), the ability of their approach to measure individual electrode impedance spectra was not evaluated.

Another way to avoid impedance artefacts due to electrode misalignment is to place a reference electrode in between the working and counter electrode rather than adjacent to it. This principle was used for studies with lithium-ion battery cells by Solchenbach et al.,[8] who placed an insulated 50 μm diameter gold wire in between two ≈200 μm thick separators that separated the anode and cathode electrode; after an initial lithiation of the gold wire, the gold wire reference electrode (Au-WRE) displayed a stable reference potential. With this configuration, artefact-free anode and cathode impedance spectra could be obtained,[8] which were later used to quantify the different impedance contributions in lithium-ion batteries.[16,17]

Therefore, in this study we developed a reference electrode, consisting of an insulated Pt-wire, which is laminated between two Nafion® 212 membranes and, thus, is centrally placed in the active area. The potential of the Pt-WRE is found to be controlled by the ratio of the permeation flux of H_2 and O_2 at the tip of the Pt-WRE that depends on the elecrolyzer current density (similar to the potential of the Pt ring electrode used by Sorsa et al.[9]). While it thus only allows for a semi-quantitative determination of the electrolyzer anode and cathode potential, the Pt-WRE is sufficiently stable to serve as pseudo-reference electrode to record artefact-free anode impedance spectra under so-called blocking conditions, i.e., when the anode charge transfer resistance becomes very large. Under these conditions, the proton conduction resistance and the capacitance of the anode electrode as well as the contact resistance at the anode||PTL interface can be quantified. Monitoring these quantities over the course of the above described OCV-AST shows that it is indeed a build-up of a contact resistance at the anode||PTL interface rather than cationic contamination that leads to the observed performance degradation during this test.

Experimental

Membrane electrode assembly (MEA) preparation and cell assembly.—Using the decal transfer method, MEAs with an active area of 5 cm^2 were prepared, where IrO_2 supported on TiO_2 (IrO_2/TiO_2 with 75 wt.-% iridium, Elyst Ir75 0480 from Umicore, Germany) served as the catalyst for the oxygen evolution reaction (OER) at the anode electrode and platinum supported on Vulcan XC72 carbon (45.8 wt.-% Pt/C, TEC10V50E from Tanaka, Japan) as the catalyst for the hydrogen evolution reaction (HER) at the cathode electrode. For ink preparation, de-ionized (DI) water (18 MΩ cm), 2-propanol (purity ⩾ 99.9% from Sigma Aldrich), and Nafion® ionomer solution (20 wt.-% ionomer, D2021 from IonPower, USA) were added to the respective amount of catalyst powder. Using a roller mill, the catalyst ink was mixed together with ZrO_2 grinding balls (5 mm diameter) for 24 h. Via the Mayer rod technique the ink was coated onto a thin decal transfer substrate (PTFE, 50 μm thick, from Angst+Pfister, Germany); after drying at room temperature, 5 cm^2 decals were punched from the coated decals. The actual weight of the electrodes was determined by weighing the decals before and after the electrode transfer step onto the membrane by hot-pressing. The following anode and cathode loadings/compositions were used in this study: 0.3 ± 0.1 mg_{Pt} cm^{-2}_{geo} for the cathode electrode with an ionomer to carbon weight ratio of 0.6/1 g_{Ion}/g_C, and 2.0 ± 0.1 mg_{Ir} cm^{-2}_{geo} for the anode electrode with an ionomer content of the electrode of 8 wt.%.

A 50 μm Pt-wire with a 9 μm PTFE insulation (Goodfellow, Great Britain) was used a reference electrode. To ensure good electrical and ionic contact, ≈1 cm of the insulation was removed at both ends of the wire. One end of the wire was then placed centrally in between two Nafion® 212 membranes (50 μm thick, from Quintech, Germany) and hot pressed together with the cathode and anode decals (see above) at 155 °C for 3 min at a pressure of 2.5 MPa. In order to protect the Pt-wire at the interface with the cell hardware, an additional layer of PP foil (40 μm from Profol Germany,) was hot pressed at this spot.

Sintered titanium (from Mott Corporation, USA) with a porosity of ≈50% and a thickness of 280 ± 10 μm was used as a porous transport layer (PTL) on the anode, whereas a carbon fiber paper (TGP-H 120 from Toray, no MPL) with a thickness of 370 ± 10 μm was used on the cathode. The MEA and PTLs were placed between the flow-fields of the electrolyzer cell and sealed with virgin PTFE gaskets (from Reichelt, Germany). By choosing the right thickness of the gaskets, a compression of the carbon PTL by 25% was set, corresponding to a compressive force of ≈1.7 MPa at the MEA (note that at ≈1.7 MPa, the titanium PTL and the MEA are essentially incompressible). Specific details about the cell hardware are reported elsewhere.[18]

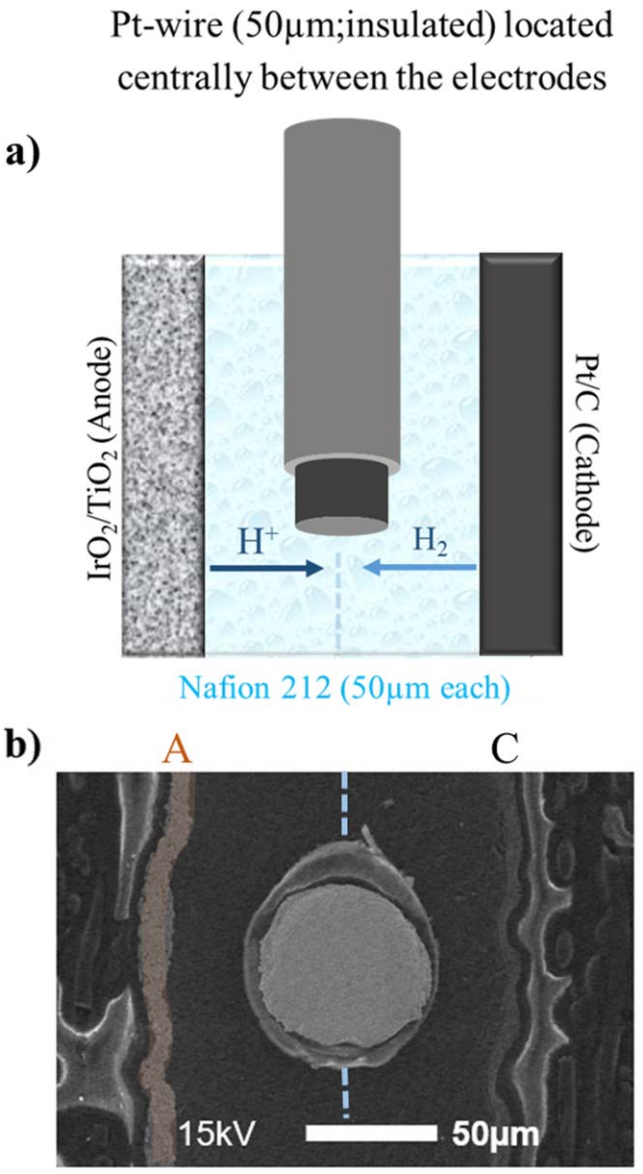

Figure 1. (a) Sketch of an MEA with a Pt-WRE, illustrating the placement of the Pt-wire and the prevailing environment at OCV with hydrogen being purged through the cathode compartment and water through the anode compartment. (b) Cross-sectional SEM image of an MEA including a 50 μm Pt-WRE laminated between two 50 μm Nafion® membranes.

Electrochemical characterization.—An automated test station from Greenlight Innovation with a potentiostat equipped with a current booster (BioLogic VSP 300) was used to perform all electrochemical measurements. The anode was supplied with 5 ml_{H2O} min^{-1} deionized (DI) water that was pre-heated to 80 °C. During the measurements, the cell temperature was kept constant at 80 °C, and the product gas exiting from the anode side was diluted with nitrogen (100 nccm) to avoid the formation of an explosive gas mixture due to hydrogen permeation through the membrane into the anode compartment. During warm-up, the cathode was flushed with N_2 for 300 s while supplying 5 ml_{H2O} min^{-1} to the anode compartment. After reaching the desired cell temperature of 80 °C, dry H_2 (50 nccm) at ambient pressure was supplied to the cathode in order to assess the functionality of the reference electrode. Since no current was applied and, hence, no oxygen is produced under these conditions, the potential of the Pt-WRE has to be 0 V on the reversible hydrogen electrode (RHE) potential scale, so that the potential between the H_2-purged electrolyzer cathode and the Pt-WRE must be 0 V, indicating proper electrical contact and isolation of the Pt-WRE. Afterwards, the cell was conditioned at 1 A cm^{-2}_{geo} for 30 min. Subsequently, potential-controlled polarization curves were taken at ambient pressure (1 bar_a) and 80 °C, stepwise increasing the cell potential from 1.3 to 1.9 V and holding at each potential for 15 min to ensure a stabilization of the electrolyzer current density. Finally, the last 10 s of both the cell voltage and current density were averaged for each point.

The OCV-AST was conducted at 80 °C with a cathode pressure of 10 bar_a and ambient pressure at the anode. Each OCV-AST cycle consisted of 10 min holds at 3 A cm^{-2}_{geo}, at 0.1 A cm^{-2}_{geo}, and at OCV. After each OCV-hold, the potential was set to 1.3 V to perform impedance measurements in blocking conditions (see below). The flow of H_2O through the anode compartment and the cell temperature were kept constant also during the OCV- or the 1.3 V-hold periods.

Impedance measurements (100 kHz to 1 Hz) were performed at the end of each potential step in the potentiostatic polarization curves, using 10 mV amplitude of the potential perturbation. In the case of the OCV-AST, impedance measurements (100 kHz to 1 Hz) were performed at the end of each current step, using a current perturbation amplitude that was set 500 mA for 3 A cm^{-2}_{geo} and 60 mA for 0.1 A cm^{-2}_{geo}. In addition, after each OCV-cycle, a potentiostatic impedance spectrum (100 kHz to 1 Hz) was acquired at 1.3 V, using 10 mV amplitude of the potential perturbation. During the impedance measurement at 1.3 V the temperature was kept at 80 °C and the pressure of the cathode was held at 10 bar_a. The high-frequency resistance (HFR) was determined from the high-frequency intercept with the real axis in a Nyquist plot or by fitting a transmission line model to the anode impedance spectra as described in the section *Evaluation of the Impedance Spectra by Fitting a Transmission Line Model*. Using a Matlab based application ("EIS Breaker," © J. Landesfeind), which is based on the fminsearch MATLAB function using a Nelder-Mead simplex algorithm and modulus weighing, the impedance spectra were fitted. The scaled difference between the measured data and fit vectors $\left(\frac{|Z(f_i)| - |Z_{fit}(f_i)|}{|Z_{fit}(f_i)|}\right)$ at the same frequency f_i were used to calculate the residuals (in %).

At the beginning-of-test (BoT) and at the end-of-test (EoT) of the OCV-AST, cyclic voltammograms (CVs) of the anode electrode were recorded. For this, the test procedure was stopped after the 1.3 V-hold period, and the cathode counter electrode was flushed with dry H_2 at 50 nccm at ambient pressure to ensure a stable reference potential (i.e., the cathode served as counter and reference electrode in this case), while the anode electrode was continuously fed with 5 ml_{H2O} min^{-1} deionized water. The CVs were recorded in a potential range of 0.05 V–1.3 V at 50 mV s^{-1} at 80 °C; shown are the steady-state CVs (2nd one recorded).

Physical characterization.—Using a JEOL JCM6000Plus NeoScope scanning electron microscope at an accelerating voltage of 15 kV, cross-sectional scanning electron microscopy (SEM) micrographs were obtained to depict the location of the Pt-wire reference electrode. The SEM samples were prepared by embedding the MEA in a room-temperature curing epoxy and drying over night at 80 °C. Afterwards, the sample surface was ground using a SiC paper in two steps (grade P320 and P1200, from Buehler, Germany) and subsequently polished on a microcloth using a 9 μm diamond polishing agent.

Results

Implementation and validation of the Pt-wire reference electrode.—By implementing an additional reference electrode—normally the cathode is serving as counter and reference electrode at the same time—it is possible to analyze both half-cells individually.[8,11,14] However, certain requirements must be met when the impedance of both half-cells is to be measured: i) the reference potential should be of a well-defined value for a true reference

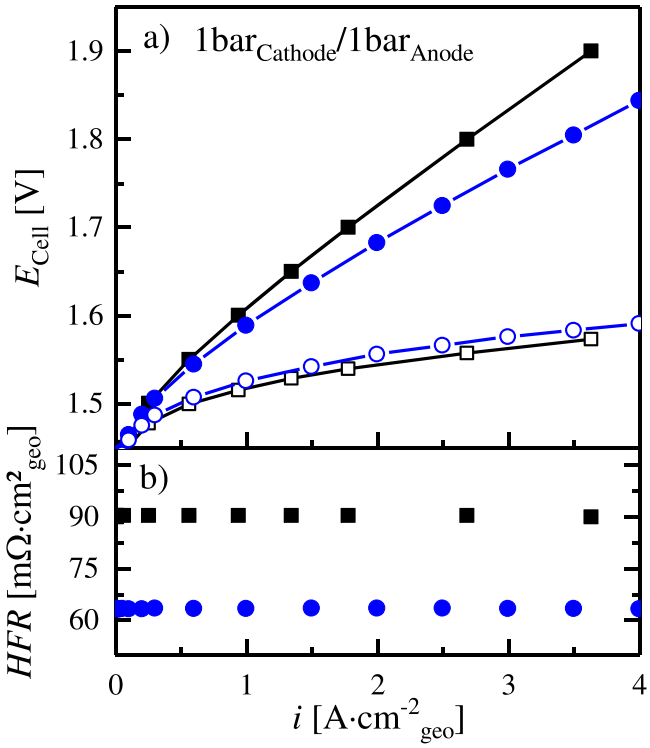

Figure 2. PEM-WE performance data at 80 °C and ambient pressure for an MEA including a Pt-WRE (100 μm membrane, black squares) and an MEA with a single 50 μm Nafion® membrane (blue circles): (a) cell voltage (E_{cell}) vs current density (i) performance (filled symbols) and HFR-corrected performance data (hollow symbols); (b) corresponding HFR values (extracted from the intercept in the Nyquist plot). MEA specifications: 5 cm^2 active-area with ≈2 mg$_{Ir}$ cm$^{-2}_{geo}$ anode and ≈0.3 mg$_{Pt}$ cm$^{-2}_{geo}$ cathode loading.

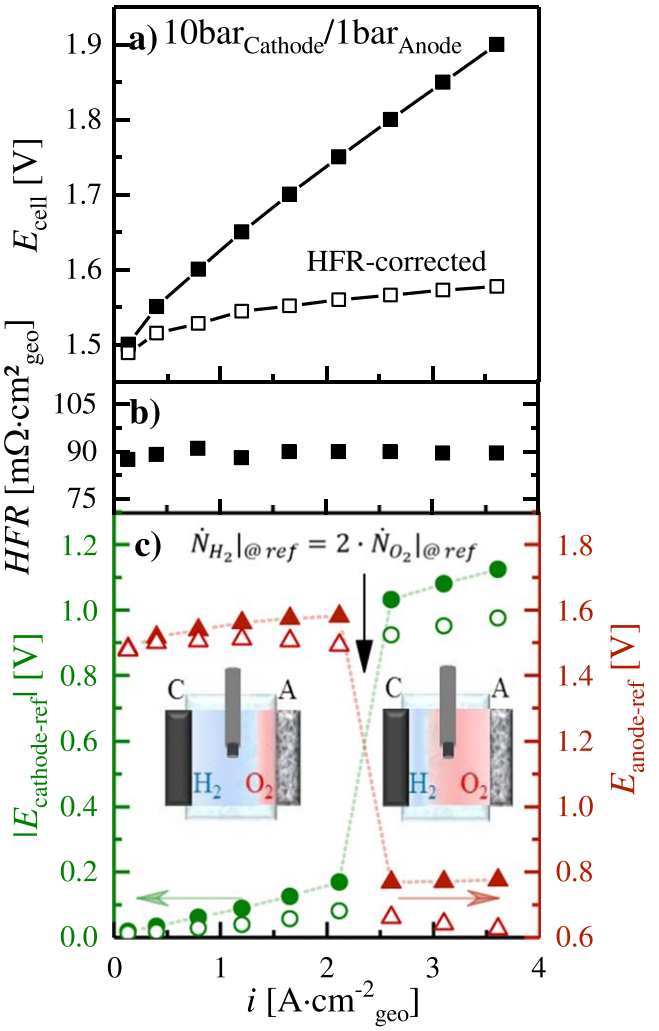

Figure 3. PEM-WE performance data at 80 °C recorded with the Pt-WRE MEA based on two 50 μm Nafion® membranes (see Fig. 1) at a cathode pressure of 10 bar$_a$ and an anode pressure of 1 bar$_a$: (a) E_{cell} vs i performance (filled symbols) and HFR-corrected performance data (hollow symbols); (b) corresponding HFR values (extracted from the high-frequency intercept with the real axis in the Nyquist plot). (c) Potential difference between the anode electrode and the Pt-WRE ($|E_{anode-ref}|$; solid red triangles, plotted vs the right y-axis) and absolute potential difference between the cathode electrode and the Pt-WRE ($|E_{cathode-ref}|$; solid green circles, plotted vs the left y-axis); the open circles and triangles represent a correction of these potentials by the ohmic potential drop through a single 50 μm membrane (i.e., by i × 40 mΩcm$^2_{geo}$). The inset shows sketches depicting the prevalent local gas composition at the Pt-WRE tip at high (>2 Acm$^{-2}_{geo}$, right sketch) and low current densities (<2 Acm$^{-2}_{geo}$, left sketch). MEA specification: 5 cm^2 active-area with ≈2 mg$_{Ir}$ cm$^{-2}_{geo}$ anode and ≈0.3 mg$_{Pt}$ cm$^{-2}_{geo}$ cathode loading.

electrode; ii) however, even if the potential of the reference electrode is not well-defined (e.g., if it varies with the operating conditions), as long as its potential is stable over the course of an impedance measurement, it can be used as pseudo-reference electrode; iii) the reference electrode should be placed centrally between the two electrodes in order to avoid the edge effects that were discussed in the introduction section.[8,19,20] To address the last point, an approach already well established for lithium-ion battery cells[8,16,17] was adapted to the MEA of a PEM-WE. A 50 μm thick Pt-wire was laminated between two 50 μm Nafion® membranes that were coated with the respective anode or cathode catalyst layer; the tip of the Pt-wire was located at the center of each catalyst layer. As illustrated by the sketch in Fig. 1a and by the SEM cross-section of the MEA in Fig. 1b, the Pt-wire is located centrally between the two half-cell membranes, without bending towards either side of the MEA. A bending of the Pt-wire towards one of the electrodes can cause a disturbance of the impedance measurement due to an inhomogeneous current distribution or, in the worst case, a shortening of the cell.

The following experiments are aimed to verify that the Pt-WRE does not affect the overall electrolysis performance of the MEA. Figure 2a shows the performance curves measured at ambient pressure for the MEA with the Pt-WRE laminated between two 50 μm Nafion® membranes used in this study (black squares) compared to an MEA with the same catalyst loadings but only a single 50 μm Nafion® membrane without a Pt-WRE (blue circles). The cell voltage is higher for the MEA with the Pt-WRE, which can be attributed to its higher HFR (cf Fig. 2b), as would be expected due to its overall 2-fold higher membrane thickness. Consequently, the HFR-corrected cell voltages, compensating for the differences in membrane resistance are essentially identical for the MEA with the Pt-WRE (hollow black squares in Fig. 2a) and the MEA with the single 50 μm membrane without the Pt-WRE (hollow blue circles; differing by only ≈10 mV at the highest current density). This proves that the Pt-wire does not negatively affect the cell performance. The HFR-corrected cell voltages in Fig. 2a are in excellent agreement with previous measurements by Bernt et al.[18] for Nafion® 212 based MEAs with the same catalysts and catalyst loadings.

As shown in Fig. 2b, the HFR for the MEA with the two 50 μm Nafion® membranes and the Pt-WRE is ≈90 mΩcm$^2_{geo}$. In general, the HFR is the sum of the electronic resistance (≈12 mΩcm$^2_{geo}$ for the cell hardware used in this study[18]) and the membrane resistance, which based on various literature reports ranges between ≈41–54 mΩcm$^2_{geo}$ for a single 50 μm Nafion® membrane at 80°C.[18] Assuming the lower value, the resistance of two 50 μm Nafion®

membranes should be ≈82 $m\Omega cm^2_{geo}$, predicting an overall HFR of ≈94 $m\Omega cm^2_{geo}$, which is in good agreement with the measured HFR, suggesting that the HFR is not affected by the presence of the Pt-WRE. It should be noted that the HFR of the MEA with the a single 50 μm Nafion® membrane of ≈62 $m\Omega cm^2_{geo}$ (see Fig. 2b) is somewhat higher than what we had observed previously for nominally identical MEAs (≈53–57 $m\Omega cm^2_{geo}$[6,18]), which we believe is due to slight differences in cell compression that strongly affect the contact resistance between the PTLs and the flow fields.

Next we will examine whether the potential of the Pt-WRE is independent of the current density that is applied to the electrolyzer cell. Figure 3a shows the performance curve of the Pt-WRE MEA composed of two 50 μm Nafion® membranes (i.e., with a total membrane thickness of 100 μm; see Fig. 1) measured at 80 °C with 10 bar_a cathode and and 1 bar_a anode pressure; the corresponding cell HFR values are shown in Fig. 3b. Again, while the cell voltage performance (black squares in Fig. 3a) is worse compared to that obtained with an otherwise identical MEA with a single 50 μm Nafion® membrane that was reported by Bernt et al.,[18] the HFR-corrected performance (hollow squares in Fig. 3a) of both MEA types is essentially identical (e.g., at 3 Acm^{-2}_{geo} the cell voltage is ≈1.56 V in Fig. 3a vs ≈1.55 V in Ref. 18). This proves that the Pt-wire does not affect the cell performance, even when operated at differential pressure.

Figure 3c shows the half-cell potentials recorded during the polarization curve in Fig. 3a, namely the absolute value of the difference between the cathode and the Pt-WRE potential ($|E_{cathode-ref}|$; solid green circles plotted vs the left *y*-axis) and the difference between the anode and the Pt-WRE potential ($|E_{anode-ref}|$; solid red triangles plotted vs the right *y*-axis). It is most straightforward to first discuss the $|E_{cathode-ref}|$ values as a function of current density. As was shown previously, the potential of an electrolyzer cathode at high Pt loadings of ≈0.3 $mg_{Pt}\ cm^{-2}_{geo}$ is expected to remain within ⩽ 10 mV vs RHE up to 3 Acm^{-2}_{geo} due to the fast HER kinetics[18] so that the cathode potential under the conditions in Fig. 3 can be considered essentially constant. At the same time, the potential of the Pt-WRE is a mixed potential resulting from the simultaneous electrochemical oxidation of H_2 and the reduction of O_2, both of which are dissolved in the membrane phase. As a consequence, the potential of the Pt-WRE depends on the relative permeation fluxes of H_2 ($\dot{N}_{H_2(x)}$) and O_2 ($\dot{N}_{O_2(x)}$) at the location of the Pt-WRE, and Takaichi et al. showed that the potential of a membrane-embedded Pt-wire jumps from near 0 V_{RHE} to ≈0.8–0.9 V_{RHE} when $\dot{N}_{H_2(x)} < 2 \times \dot{N}_{O_2(x)}$ at the location of the Pt-wire[21] (the same potential transition of a membrane-embedded Pt-wire was also observed by Liu and Zuckerbrod[22]). Since the permeability of H_2 through a Nafion® membrane is ≈2 fold higher than the permeability of O_2,[22,23] the potential of a Pt-wire embedded halfway through the thickness of a membrane (as is the case for our Pt-WRE) would be near the potential transition region when the partial pressures of H_2 and O_2 are equal; in this case, the molar flux of H_2 at the Pt-WRE would be twice as high as the molar flux of O_2, allowing for the complete conversion of both of the dissolved gases to H_2O. On the other hand, for the differential pressure conditions used in Fig. 3 ($p_{anode} = 1\ bar_a$ and $p_{cathode} = 10\ bar_a$), the H_2 partial pressure of $p_{H2} \approx 9.5$ bar ($p_{H2} = p_{cathode} - p_{H2O}$, with $p_{H2O} \approx 0.5$ bar at 80 °C) is nearly 20-fold higher than the O_2 partial pressure of $p_{O2} \approx 0.5$ bar, so that the mixed potential of the Pt-WRE should be very close to 0 V_{RHE} (actually slighlty positive of 0 V_{RHE} due to the mixed potential that derives from the reduction of O_2 permeating from the anode to the Pt-WRE). Thus, based on these arguments, viz., the fast HER kinetics on Pt, the location of the Pt-WRE (see Fig. 1), and the well-known H_2 and O_2 permeabilities through Nafion®, the absolute value of the difference of the electrolyzer cathode and the Pt-WRE (i.e., $|E_{cathode-ref}|$) should be very close to 0 mV. This corresponds to a situation where residual dissolved gas at the Pt-WRE (i.e., after the stoichiometric reaction of H_2 and O_2 to H_2O) would be H_2-rich, as depicted in the left-hand sketch in Fig. 3c. At low current densities $|E_{cathode-ref}|$ is indeed very close to 0 V, as is shown in Fig. 3c (green circles).

However, as the current density increases, $|E_{cathode-ref}|$ gradually increases and then exhibits a sudden potential increase to ≈1 V between ≈2.1 and ≈2.6 Acm^{-2}_{geo}, that previously has been observed to occur once $\dot{N}_{H_2(x)}$ becomes $< 2 \times \dot{N}_{O_2(x)}$. This implies that $\dot{N}_{H_2(x)}$ and $\dot{N}_{O_2(x)}$ must be a function of current density. Based on previous measurements, the H_2 permeation flux from cathode to anode in a PEM-WE operated at cathode/anode pressures of 10/1.0 bar_a remains essentially constant between 0 to 2 Acm^{-2}_{geo}.[24] On the other hand, the O_2 permeation flux for an electrolyzer operated at cathode/anode pressures of 1.0/1.0 bar_a was reported by Trinke et al. to increase by ≈20-fold when the current density increases from 0 to 2 Acm^{-2}_{geo}.[25] Thus, beyond this current density, where based on these literature reports $\dot{N}_{H_2(x)}$ would become $< 2 \times \dot{N}_{O_2(x)}$ (viz., at ≈2 Acm^{-2}_{geo}[24]), the expected residual dissolved gas at the location of the Pt-WRE would be O_2-rich (see right-hand sketch in Fig. 3c) and the Pt-WRE potential should increase to ≈0.8–0.9 V vs RHE.[21,22] This is actually in very good agreement with the observed rapid increase of $|E_{cathode-ref}|$ near 2 Acm^{-2}_{geo}[24] shown in Fig. 3c. Besides the large expected change in the $\dot{N}_{H_2(x)}/\dot{N}_{O_2(x)}$ ratio and its effect on $|E_{cathode-ref}|$, a minor effect to consider is that the potential drop across the membrane segment between the cathode electrode and the Pt-WRE when drawing an electrolyzer current must also be considered, as it will add an additional ohmic potential drop, corresponding to the areal resistance of the 50 μm Nafion® membrane (≈40 $m\Omega cm^2_{geo}$, as discussed in the context of Fig. 2) multiplied by the electrolyzer current density. The $|E_{cathode-ref}|$ values corrected by the ohmic potential drop are shown by the open green circles in Fig. 3c, amounting to ≈0.92–0.98 V at ≈2.6–4.6 Acm^{-2}_{geo}, consistent with the values reported for membrane-embedded Pt-wires at conditions where $\dot{N}_{H_2(x)} < 2 \times \dot{N}_{O_2(x)}$.[21,22]

In summary, prior to the transition region of the Pt-WRE potential, its potential corrected by the ohmic potential drop (open green circles) ranges between ≈10–100 mV_{RHE} and will thus allow a rough assignment of the cathode potential. It has to be noted, however, that the potential of the Pt-WRE is influenced by the oxygen crossover and thus the oxygen reduction, even before the transition point (≈2.1 and ≈2.6 Acm^{-2}_{geo}) occurs. Thus the observed increase in $|E_{cathode-ref}|$ is most likely caused by a mixed potential of the Pt-WRE, that derives from the reduction of O_2 permeating from the anode to the Pt-WRE as well as the oxidation of the hydrogen permeating from the the cathode to the Pt-WRE, rather than by the charge transfer kinetics of the HER on the cathode. Beyond the transition region, its ohmic potential drop corrected value is at ≈0.9–1.0 V_{RHE}. Owing to the significant current density dependence of the Pt-WRE potential during electrolyzer operation, artefact-free individual electrode resolved impedance spectra cannot be obtained during electrolyzer operation, as the variation of the H_2 and O_2 partial pressures at the catalyst||membrane interface during the impedance measurements leads to a simultaneous perturbation of the Pt-WRE, which in turn results in inductive loops of the individual impedance spectra,[26] similar to those observed by Sorsa et al.[9] However, at very low current densities (at/near the OCV), this effect is negligible and artefact-free individual electrode impedance spectra can be obtained, as will be shown later.

Figure 3c also shows the anode potentials referenced to the Pt-WRE ($|E_{anode-ref}|$; solid red triangles plotted vs the right *y*-axis), and the same considerations apply: at low current densities, the anode potential can be determined by the Pt-WRE using the $|E_{anode-ref}|$; values corrected by the ohmic potential drop (open red triangles), with an error that is increasing with current density and ranges between ≈1.47–1.51 V.

As a side note, it should be mentioned that the current density at which the potential transition region of the Pt-WRE occurs can

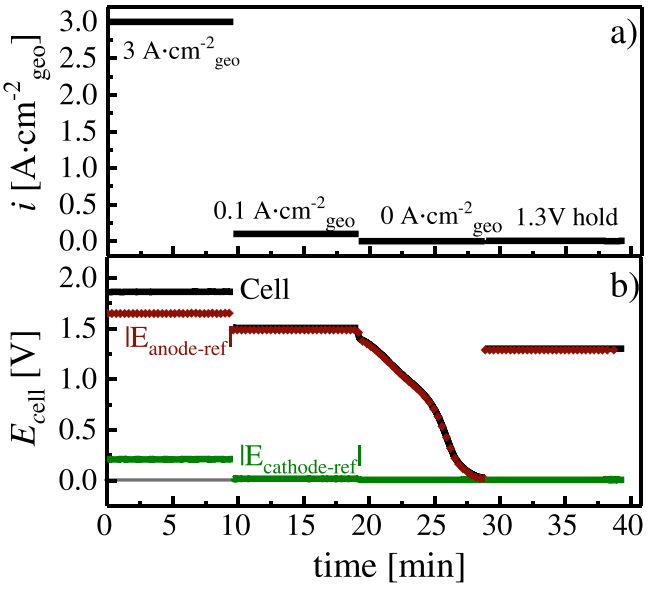

Figure 4. First cycle of the OCV-AST recorded with the Pt-WRE MEA based on two 50 μm Nafion® membranes (see Fig. 1), conducted at 80 °C with cathode/anode pressures of 10/1.0 bar_a and with a continuous feed of 5 ml $_{H2O}$ min^{-1} into the anode compartment. (a) Current profiles, with high and low current density periods followed by an idle period at OCV, mimicking electrolyzer operation with a fluctuating renewable energy source as well as a potential hold at 1.3 V to record an impedance spectrum. (b) Associated profiles of the cell voltage (black line) as well as of the half-cell potentials, described by the potential difference between the anode electrode and the Pt-WRE ($|E_{anode-ref}|$; red triangles) and by the absolute potential difference between the cathode electrode and the Pt-WRE ($|E_{cathode-ref}|$; green line). MEA specification: 5 cm^2 active-area with ≈2 mg_{Ir} cm^{-2}_{geo} anode and ≈0.3 mg_{Pt} cm^{-2}_{geo} cathode loading.

provide a means to quantify the oxygen permeation rate at this current density, since at this point $\dot{N}_{H_2(x)} = 2\times\dot{N}_{O_2(x)}$. Based on the results of Bernt et al., the hydrogen permeation flux through a 50 μm Nafion® 212 membrane at 80 °C and a cathode pressure of 10 bar_a is $\approx 0.54\frac{mmol}{m^2 s}$ at a current density of ≈2 Acm^{-2}_{geo}.[24] As the potential transition region occurs at/near this current density, the corresponding oxygen permeation flux must be $\approx 0.27\frac{mmol}{m^2 s}$. By applying different combinations of anode and cathode pressures and determining the current density at which the potential transition occurs, the oxygen permeation flux through the membrane can be determined if the H_2 permeation flux is known (the latter is relatively easy to quantify).[24] However, this was beyond the scope of this work and will not be discussed further.

Open circuit voltage—accelerated stress test (OCV-AST).—In a previous study we proposed an accelerated degradation test protocol to determine whether cycles between load and OCV conditions would lead to MEA and/or OER catalyst degradation.[6] Figure 4a depicts one cycle of the OCV-AST test protocol, where current densities of 3 Acm^{-2}_{geo} and 0.1 Acm^{-2}_{geo} alternate with idle periods where no current is supplied and the cell is left at OCV, mimicking the operation of an electrolyzer with fluctuating renewable energy sources. Figure 4b shows the corresponding cell voltage of the electrolyzer as well as the half-cell potentials, plotted here for the very first cycle. The cell voltage (black line) remains essentially constant during operation and the cell voltages are in good agreement with the polarization curve at the respective current density that was shown in Fig. 3a. However, upon current interruption (i.e., during the OCV phase), the cell voltage gradually decreases to ≈0 V within ≈10 min which we attributed to an accumulation of hydrogen within the anode compartment via hydrogen permeation through the membrane from the cathode

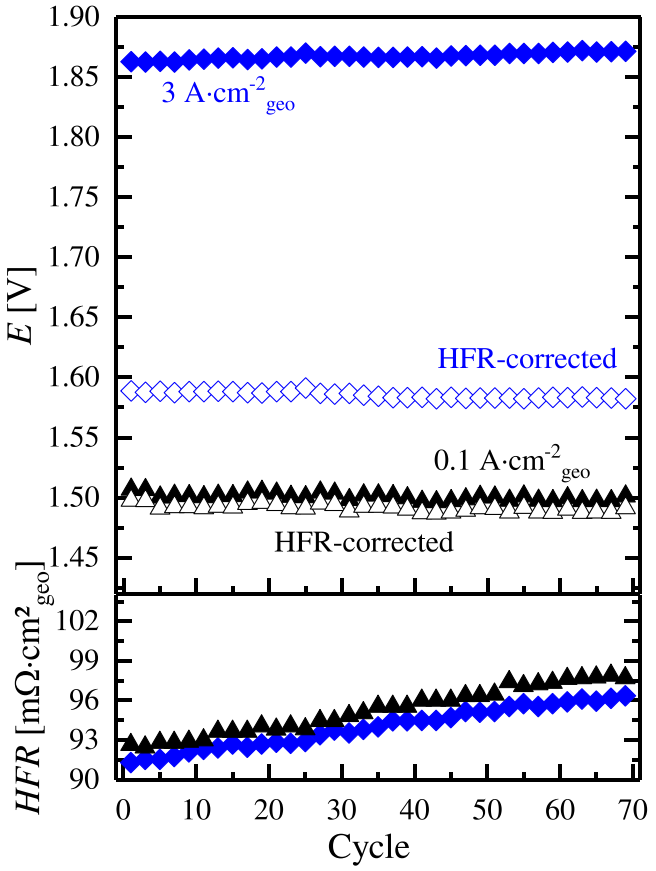

Figure 5. (a) Evolution of the cell voltage and the full-cell HFR-corrected cell voltage at 0.1 Acm^{-2}_{geo} and 3 Acm^{-2}_{geo} during the OCV-AST with the Pt-WRE MEA based on two 50 μm Nafion® membranes (see Fig. 1). The test was conducted at 80 °C with $p_{cathode}$ = 10 bar_a and p_{anode} = 1 bar_a,, cycling the cell with the protocol shown in Fig. 4a while feeding 5 ml_{H2O} min^{-1} into the anode compartment (same MEA specifications as in Fig. 4). (b) Corresponding full-cell HFR values. For better legibility, only every 2nd point was plotted.

compartment that was kept at a high H_2 pressure (≈10 bar_a), concomitant with a lowering of the anode potential to ≈0 V vs RHE due to the reduction of IrO_2 and the concomitant formation of metallic iridium, which is catalytically active towards the hydrogen oxidation reaction (HOR).[6]

To verify the above hypothesis, the OCV-AST was repeated with a Pt-WRE MEA with the same catalysts and catalyst loadings but with a thicker membrane (two 50 μm Nafion® membranes rather than one) in order to enable a determination of the cathode and anode half-cell potentials. Particularly at low current densities, the half-cell potentials can be determined quite accurately, since the Pt-WRE potential will be within ≈10–20 mV_{RHE} for <0.4 Acm^{-2}_{geo} (see green circles in Fig. 3c). Thus, at 0.1 and 0 Acm^{-2}_{geo} during the OCV-AST, the potential difference between the anode electrode and the Pt-WRE ($|E_{anode-ref}|$; see triangles in Fig. 4b) as well as the absolute potential difference between the cathode electrode and the Pt-WRE ($|E_{cathode-ref}|$; see green line) will represent the anode and cathode potentials vs RHE with an error of less than ≈20 mV. Based on this, Fig. 4b clearly shows that during the OCV period the cathode potential remains at ≈0 V_{RHE}, while the anode potential drops to ≈1.3 V_{RHE} right at the beginning of the OCV period (roughly corresponding to the reversible cell voltage under these conditions) and then gradually decreases to ≈0 V_{RHE} at the end of the OCV period. This gradual decrease in anode potential is attributed to the enrichment of hydrogen within the anode compartment via H_2 permeation from the pressurized cathode compartment through the membrane to the anode compartment. As the cathode

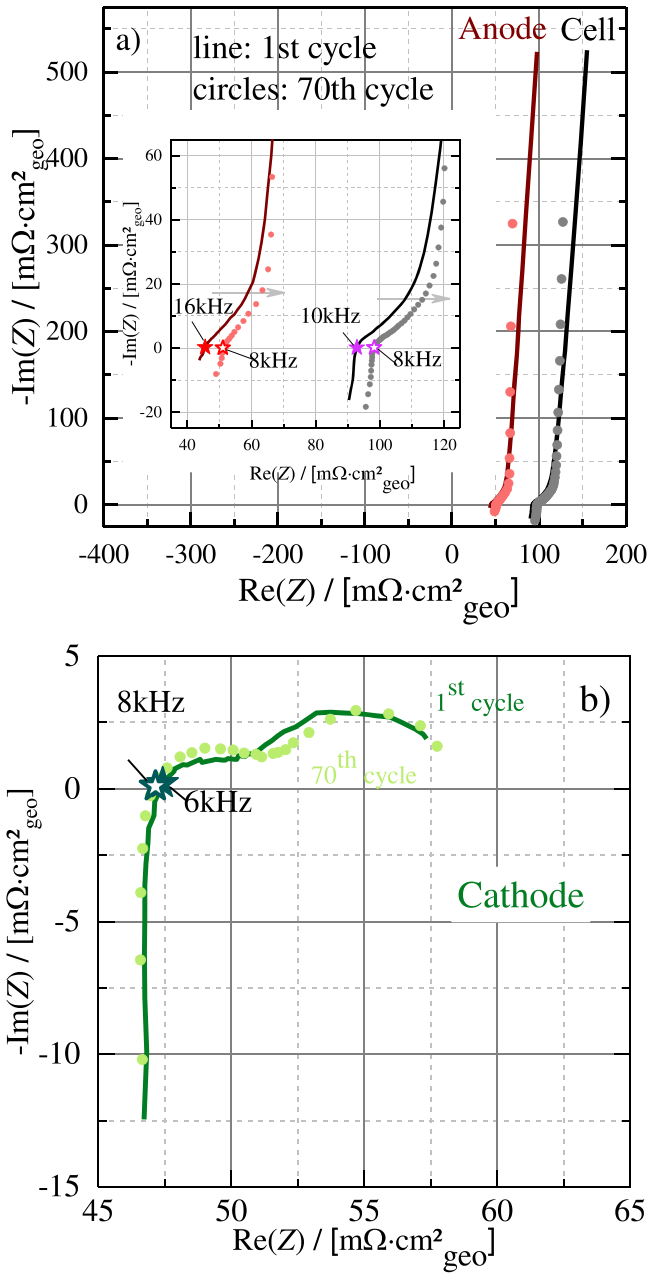

Figure 6. Electrochemical impedance spectra recorded at an electrolyzer voltage of 1.3 V and 80 °C (see Experimental section) over the course of the OCV-AST shown in Fig. 4, namely after the 1st (solid lines) and after the 70th (circles, plotting every 2nd data point for better visibility) OCV-AST cycle. (a) Full-cell impedance spectra (black line/circles) and anode impedance spectra taken with respect to the Pt-WRE (red line/circles); the inset is a magnification of the high-frequency regions of the spectra. (b) Cathode impedance spectra taken with respect to the Pt-WRE (green line/circles). The stars mark the real-axis high-frequency intercepts (and the corresponding frequencies) which are commonly used to determine the HFR (e.g., the full-cell HFR shown in Fig. 5b).

pressure is not released during the OCV period of our OCV-AST, a high H_2 partial pressure of ≈9.5 bar in the cathode compartment will be maintained during the OCV period, resulting in a high H_2 permeation rate of ≈0.54 mmol $m^{-2}s^{-1}$.[24] As a result, a hydrogen-rich gas-phase is developing at the anode side, causing a gradual reduction of the outermost surface of the IrO_2 phase of the IrO_2/TiO_2 OER catalyst to metallic iridium that is catalytically active for the hydrogen oxidation reaction (HOR).[6,27–30] Finally, once a sufficient HOR activity is established, the anode voltage will drop rapidly close to the equilibrium potential for the HOR at ≈0 V_{RHE}. This clearly confirms our previous hypothesis that the potential of the anode electrode decreases to ≈0 V_{RHE} over the course of the OCV period of our OCV-AST.

On a side note, it should be mentioned that based on Fig. 3 one would have expected that $|E_{cathode\text{-}ref}|$ should be positive of 1 V at 3 Acm^{-2}_{geo}, instead of the ≈0.21 V observed in Fig. 4b. This is due the fact that the potential of the Pt-WRE is extremely sensitive to pressure fluctuations at current densities that are close to the transition region of the Pt-WRE; as a consequence, even under nominally identical conditions, small variations in cathode/anode pressure shift the current density range in which the Pt-WRE potential transition occurs (found to be at ≈2.1–2.6 Acm^{-2}_{geo} in Fig. 3 and at >3 Acm^{-2}_{geo} in Fig. 4).

Figure 5a shows the cell voltage evolution over the first 70 cycles of the OCV-AST with the Pt-WRE MEA at the two different current densities of 0.1 Acm^{-2}_{geo} (black triangles) and 3 Acm^{-2}_{geo} (blue diamonds). Even after only 70 cycles, an increase in cell voltage of ≈10 mV can be observed, which is similar to that observed in our previous study,[6] although the absolute cell voltage (≈1.86 V) is higher in the present study due to the larger membrane thickness (MEA based on two 50 μm Nafion® membranes vs one 50 μm Nafion® membrane, with identical catalysts and catalyst loadings). Compared to the performance at 3 Acm^{-2}_{geo}, the cell performance at 0.1 Acm^{-2}_{geo} (black triangles) remained essentially unchanged during the 70 OCV-AST cycles (≈1.5 V). Here it must be noted that the initial increase in performance during the first 10 OCV-AST cycles that we had observed in our previous study (cf Fig. 2b from Weiß et al.[6]) was not observed in the present study, which we believe is due to the Pt-WRE functionality test at 80 °C prior to the OCV-AST, where hydrogen was purged through the cathode compartment while water was purged through the anode compartment without drawing any electrolysis current for some extended time. This exposure of the MEA to hydrogen in the absence of oxygen evolution leads to a hydrogen-rich environment in the anode compartment and a concomitant reduction of the crystalline IrO_2 phase of the anode catalyst to a more OER active hydrous iridium-oxide phase, a process already occurring prior to initiating the OCV-AST.[29,30] As this pre-treatment was not used in our previous OCV-AST study,[6] the performance improvement associated with the formation of the more OER active hydrous iridium oxide instead occurred there over the first few cycles of the OCV-AST.

A closer look at the corresponding full-cell HFR (Fig. 5b) measured during the OCV-AST test reveals an increase of the full-cell HFR at both the high (blue diamonds; ΔHFR ≈ 5 $m\Omega cm^2_{geo}$) and the low (black triangles; ΔHFR ≈ 5 $m\Omega cm^2_{geo}$) current density. Once the cell voltage is corrected by the full-cell HFR (hollow symbols in Fig. 6a), an even slightly improving performance HFR-corrected cell performance at 3 Acm^{-2}_{geo} can be observed over 70 cycles (≈10 mV; hollow blue diamonds). This clearly shows that the decrease in cell voltage over the 70 OCV-AST cycles is caused by an increasing full-cell HFR, as was observed previously.[6]

Evaluation of the individual electrode impedance spectra.— While artefact-free impedance spectra of individual electrodes cannot be obtained with the Pt-WRE during electrolyzer operation,[26] they can be acquired when the electrolyzer current is essentially zero. Therefore, we acquired impedance data at an electrolyzer cell voltage of 1.3 V, where the electrolyzer current is close to zero (≈1 $mAcm^{-2}_{geo}$, largely caused by the oxidation of part of the hydrogen permeation flux through the membrane). Based on the known OER kinetics of IrO_2/TiO_2 that were shown to follow simple Tafel kinetics with a Tafel slope (TS) of ≈50 mV dec^{-1},[15,18] the OER current density (i_{OER}) at an electrolyzer cell voltage of 1.3 V is projected to be on the order of 0.1 $mAcm^2_{geo}$ (see Fig. 6 in Ref. 6). Using these values, the OER charge transfer resistance (R_{ct}) can be estimated from Eq. 1, resulting in a value of ≈220 Ωcm^2_{geo} at

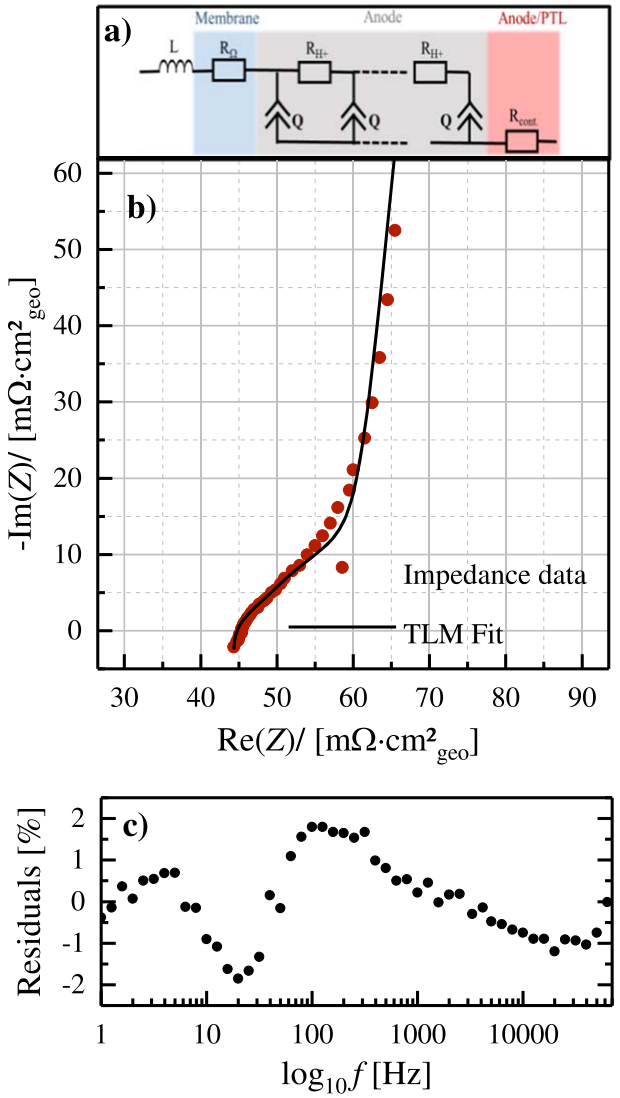

Figure 7. (a) Simplified transmission line model (TLM) to fit the anode impedance response under blocking conditions (i.e., at an electrolyzer cell voltage of 1.3 V) with the following circuit elements: i) an inductor (L) to account for the inductive behavior of the system at high frequencies; ii) a resistor (R_Ω) to represent the proton conduction resistance of the membrane between the anode electrode and the Pt-WRE; iii) a constant phase element (Q) to represent the capacitance of the anode electrode; iv) a resistor ($R_{H^+,}$) to represent the proton conduction resistance across the anode electrode; and, v) a resistor (R_{cont}) to represent the contact resistance between the anode electrode and the titanium PTL. (b) Electrochemical impedance data of the anode (red circles; same data as shown in Fig. 6a (1st cycle, red line)) recorded at an electrolyzer voltage of 1.3 V (at 80 °C, and cathode/anode pressures of 10/1.0 bar_a) and the fit of the impedance data (black line) obtained with the TLM shown in panel a. c) Residuals between the impedance data and the TLM fit as a function of frequency (see Experimental section).

an electrolyzer voltage of 1.3 V.

$$R_{ct} \equiv \frac{d\eta}{di_{OER}} = \frac{TS}{2.303 \cdot i_{OER}} \qquad [1]$$

This very large estimated anodic R_{ct}-value implies that the anode impedance spectrum recorded at an electrolyzer voltage of 1.3 V should essentially resemble a spectrum recorded under blocking conditions. In this case, the full-cell impedance spectrum would also show the same features, if the overall cathode impedance is sufficiently small,[15,18] as would be expected based on the fast HOR kinetics of the Pt/C based cathode electrode.

Figure 6a shows the full-cell impedance spectra after the 1st (black line) and after the 70th (black circles) OCV-AST cycle, indeed resembling an impedance spectrum that is governed by a blocking electrode response. A magnification of the high-frequency region of the spectra is shown in the inset of Fig. 6a, with the high-frequency intercepts with the real axis that correspond to the full-cell HFR-values shown in Fig. 5b being marked by the purple stars. Figure 6a and the inset also show the anode impedance spectra at 1.3 V recorded with the Pt-WRE after the 1st (red line) and after the 70th (red circles) OCV-AST cycle, exhibiting the expected blocking electrode response. The corresponding cathode impedance spectra are shown in Fig. 6b after the 1st (green line) and after the 70th (green circles) OCV-AST cycle, whereby the overall magnitude of the cathode impedance is very small compared to the anode and full-cell impedance. No apparent artefacts like inductive loops are observed for the anode and cathode impedance spectra acquired at 1.3 V by means of the Pt-WRE.

After the 1st OCV-AST cycle, the HFR of the anode (≈45 $m\Omega cm^2_{geo}$; see solid red star in the inset of Fig. 6a) and of the cathode (≈47 $m\Omega cm^2_{geo}$; see solid green star in Fig. 6b) sum up to ≈92 $m\Omega cm^2_{geo}$, which, within the error of measurement, agrees well with the full-cell HFR (≈93 $m\Omega cm^2_{geo}$; see solid purple star in the inset of Fig. 6a). Furthermore, the anode and cathode HFR-values are essentially identical, as would be expected for an equidistant placement of the Pt-WRE between the electrodes that was shown in Fig. 2.

In the following, we will first examine more closely the anode impedance spectra acquired with the Pt-WRE at an electrolyzer voltage of 1.3 V over the course of the OCV-AST. Owing to the high anode electrode charge transfer resistance at 1.3 V (see above), its impedance response resembles that of an electrode under blocking conditions, so that it can be fitted using a simple transmission line model (TLM). This allows for a determination of the proton conduction resistance of the anode electrode (R_{H^+}) and its capacitance (C), as was shown for PEM fuel cell cathodes[31] and for PME-WE anodes[32] using the hydrogen electrode as working and counter electrode as well as for lithium-ion battery electrodes using a micro-reference electrode.[16,17] Furthermore, the inductive response that is generally observed for electrochemical systems at high frequency can be modeled using an inductor element (L), which then allows for a more precise estimation of the anode-HFR. Thus, for fitting the anode impedance spectra, the simplified transmission line model shown in Fig. 7a was used, consisting of an inductor (L), the membrane resistance between the Pt-WRE and the anode electrode (R_Ω), a constant-phase element (Q, with its impedance defined as $Z_Q = 1/[Q \cdot (j \cdot \omega)^\alpha] 1$), a resistor ($R_{H^+,}$) representing the proton conduction resistance of the anode electrode, and a resistor ($R_{cont,}$) representing the contact resistance between the anode PTL and the anode electrode.

Figure 7b shows the anode impedance spectrum recorded at a cell voltage of 1.3 V after the first OCV-AST cycle (red circles; same data as that shown in Fig. 6a) together with the TLM fit (black line). As shown in Fig. 7c, the agreement between the impedance data and the fit is quite good, with residuals of <2% over the entire frequency range. The largest deviation between the data and the fit is observed in the 45 °—line region of the Nyquist plot that is governed by the through-plane proton conduction resistance of the electrode (R_{H^+}). A deviation between the TLM fit and the impedance data in the 45 °—line region (see Fig. 7b) was recently observed for lithium-ion battery electrodes in the presence of a non-uniform binder gradient within the electrode that leads to an inhomogeneous ionic resistance distribution across the thickness of the electrode.[33] The deviation observed here would correspond to the case where the ionic resistance increases towards the interface of the anode electrode and the anode PTL interface (see Figs. 3 and 4a in Ref. 33). The same was also observed by Reshetenko and Kulikovsky for PEM

fuel cell electrodes with an inhomogeneous ionomer distribution across the electrode.[34] While in such a case the apparent proton conduction resistance of the electrode would be lower than the true proton conduction resistance of the electrode, the rather small deviation observed in Figs. 7b and 7c is still negligible within the error of these measurements.

As mentioned before, extracting the high-frequency resistance from the high-frequency intercept of the impedance spectra with the real-axis in a Nyquist plot often results in an overestimation of the high-frequency resistance due to the inductive behavior at high frequencies. The differences in the high-frequency resistance values of the anode impedance spectra over the course of the OCV-AST, determined from either the high-frequency intercept with the real-axis ($R_{\Omega(\text{interecpt})}$) or from the TLM ($R_\Omega$, see Fig. 7a), are given in Table I.

This comparison shows that by using the high-frequency intercept of the impedance spectra with the real-axis in a Nyquist plot, the high-frequency resistance of the anode impedance spectra is overestimated by $\approx 2\ \text{m}\Omega\text{cm}^2_{\text{geo}}$ compared to a simplified transmission line model, where the inductive branch at high frequencies is considered. The overall error, however, is <5% (see Table I), so that the intercept can indeed be used as a good approximation of the high-frequency resistance.

Regarding the cathode impedance spectra shown in Fig. 6b, we already commented that the magnitude of the impedance is rather small compared to the full-cell and the anode impedance, except that the inductive response at high frequencies is similar in magnitude. Based on the well-known HOR kinetics of a Pt/C based electrode, a charge transfer resistance for a cathode loading of $\approx 0.3\ \text{mg}_{\text{Pt}}\ \text{cm}^{-2}_{\text{geo}}$, on the order of only $\approx 1\ \text{m}\Omega\text{cm}^2_{\text{geo}}$ would be expected (see appendix in Ref. 15). However, as shown by Kuhn et al., a detailed analysis of the cathode impedance response at the very small overall current density at 1.3 V would require considering the Tafel and the Volmer reaction steps of the hydrogen evolution/oxidation reactions in the impedance model,[35] in addition to the proton conduction resistance in the cathode electrode. Extracting meaningful proton conduction resistance values from such a model is not really possible, which is the reason why we did not pursue this approach. Instead, we only extracted the high-frequency resistance between the cathode electrode and the Pt-WRE from the intercept of the cathode impedance spectra at high frequencies with the real-axis of the Nyquist plot; based on the above analysis for the anode (summarized in Table I), we expect that the error induced by the inductive behavior at high frequencies will also be on the order of 5% or less for the cathode electrode.

Next we will examine the evolution of the impedance spectra acquired at a cell voltage of 1.3 V over the course of the OCV-AST shown in Fig. 5, where the full-cell HFR recorded at 0.1 and 3.0 $\text{Acm}^{-2}_{\text{geo}}$ was observed to increase by $\approx 5\ \text{m}\Omega\text{cm}^2_{\text{geo}}$ over 70 OCV-AST cycles. The full-cell impedance spectra recorded at a cell voltage of 1.3 V (see black lines/circles in the inset of Fig. 6a) show a similar, only slightly higher increase in the high-frequency intercept of $\approx 6\ \text{m}\Omega\text{cm}^2_{\text{geo}}$ over the 70 cycles (this minor difference might be due to a slightly lower through-plane membrane hydration due to reduced osmotic drag at low current densities and thus a slightly lower cell compression). An identical increase of the high-frequency intercept is observed for the anode impedance spectra acquired at a cell voltage of 1.3 V (see red lines/circles in the inset of Fig. 6a), while the high-frequency intercept of the cathode impedance spectra (see Fig. 6b) remains constant over the 70 OCV-AST cycles.

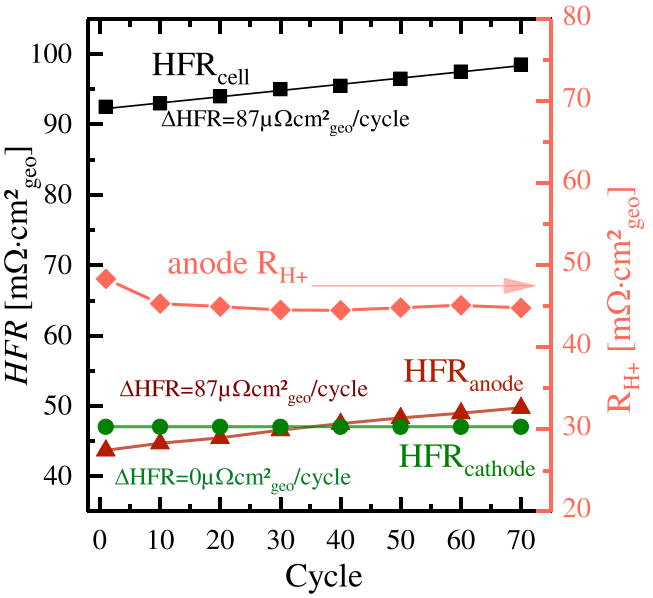

Figure 8. Evolution of the high-frequency resistances of the full-cell (HFR_{cell}, black squares), the anode ($\text{HFR}_{\text{anode}}$, red triangles), and the cathode ($\text{HFR}_{\text{cathode}}$, green circles) plotted vs the left *y*-axis, as well as of the proton conduction resistance of the anode (R_{H^+}, red diamonds, plotted vs the right *y*-axis), all determined at a cell voltage of 1.3 V, over the course of the OCV-AST shown in Fig. 4 (at 80 °C, with cathode/anode pressures of 10/1.0 bar_a). The half-cell impedances were obtained using the Pt-WRE (sandwiched between two 50 μm Nafion® membranes (see Fig. 1); same MEA specifications as in Fig. 2). HFR_{cell} and $\text{HFR}_{\text{cathode}}$ were determined by the intercept of the spectra at high frequencies with the real-axis in the Nyquist plot, while $\text{HFR}_{\text{anode}}$ was extracted by fitting the impedance spectra with the TLM shown in Fig. 7a (in this case, $\text{HFR}_{\text{anode}}$ corresponds to R_Ω in Fig. 7a). For better legibility, the data of only every 10th cycle are plotted here; the equations given in the figure are linear regression fits of the change of the HFR with the number of cycles.

Figure 8 shows the evolution of the high-frequency resistances of the full-cell (HFR_{cell}, black squares), the anode ($\text{HFR}_{\text{anode}}$, red triangles), and the cathode ($\text{HFR}_{\text{cathode}}$, green circles) acquired at a cell voltage of 1.3 V over the course of the OCV-AST (plotted vs the left-hand *y*-axis). The increase of the full-cell HFR per cycle amounts to $\Delta\text{HFR}_{\text{cell}} = 87\ \mu\Omega\text{cm}^2_{\text{geo}}\ \text{cycle}^{-1}$ and is identical with that of the anode electrode ($\Delta\text{HFR}_{\text{anode}} = 87\ \mu\Omega\text{cm}^2_{\text{geo}}\ \text{cycle}^{-1}$), while the cathode HFR is essentially zero ($\Delta\text{HFR}_{\text{cathode}} = 0\ \mu\Omega\text{cm}^2_{\text{geo}}\ \text{cycle}^{-1}$). This clearly proves that the increase in the full-cell HFR during the OCV-AST can be ascribed solely to the anode side of the MEA.

Figure 8 also shows the proton conduction resistance of the anode electrode (R_{H^+}, red diamonds, plotted vs the right-hand *y*-axis) determined at a cell voltage of 1.3 V from the fit of the anode impedance spectra using the TLM shown in Fig. 7a. Clearly, the

Table I. Comparison of the high-frequency resistance values determined from the anode impedance spectra over the course of the OCV-AST shown in Fig. 4, either from the high-frequency intercept of the impedance spectra with the real-axis in the Nyquist plot ($R_{\Omega(\text{interecpt})}$) or from a fit to the TLM shown in Fig. 7a (R_Ω).

	1st cycle	10th cycle	20th cycle	40th cycle	60th cycle
$R_{\Omega(\text{interecpt})}$ [$\text{m}\Omega\text{cm}^2_{\text{geo}}$]	45.5	46.5	47.5	48.5	50.0
R_Ω from the TLM [$\text{m}\Omega\text{cm}^2_{\text{geo}}$]	43.6	44.6	45.4	47.4	48.9
$(R_{\Omega(\text{interecpt})} - R_\Omega)/R_\Omega$ [%]	+4.4%	+4.3%	+4.6%	+2.3%	+2.2%

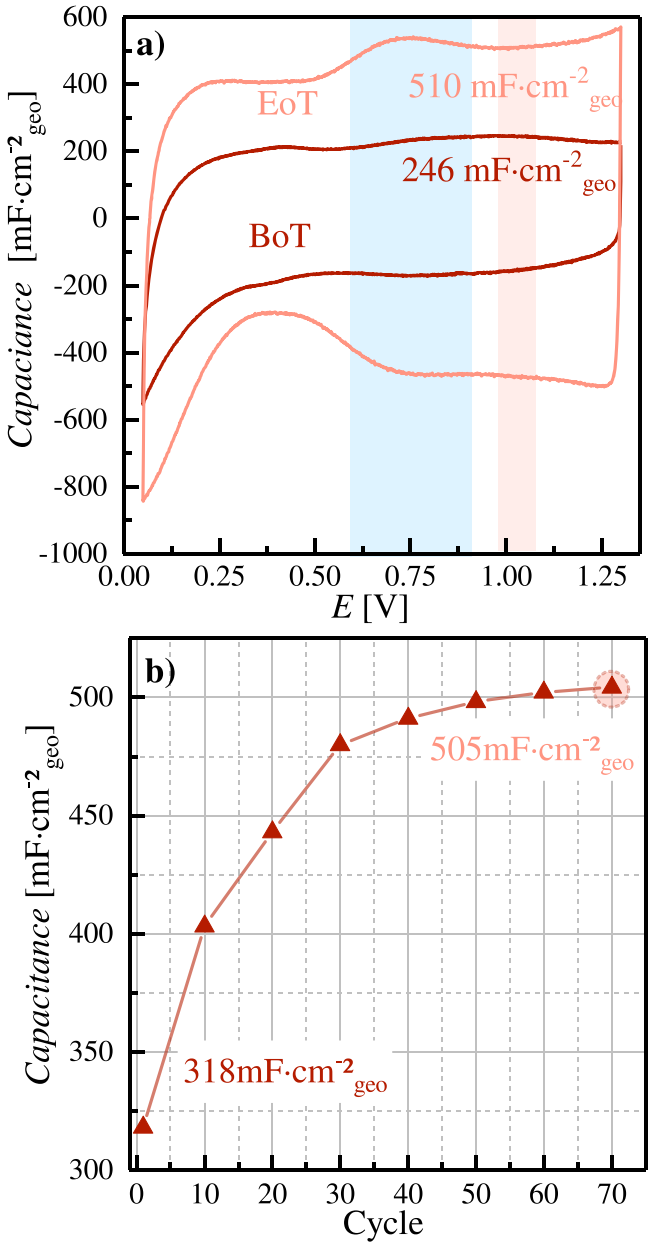

Figure 9. (a) Cyclic voltammograms recorded at beginning-of-test (BoT, i.e., prior to the OCV-AST) and at end-of-test (EOT, i.e., after the 70 OCV-AST cycles shown in Fig. 5), recorded at 50 mV s^{-1}, 80 °C, and ambient pressure, with 5 ml_{H2O} min^{-1} supplied to the anode and 50 nccm H_2 to the cathode. (b) Anode capacitance values extracted from the anode impedance spectra at 1.3 V_{cell} over the course of the OCV-AST test, using the TLM shown in Fig. 7a.

proton conduction resistance of the anode remains almost constant over the course of the 70 OCV-AST cycles, decreasing slightly from initially ≈48 mΩcm$^2_{geo}$ to ≈45 mΩcm$^2_{geo}$ after 70 OCV-AST cycles. The absolute value of the anode R_{H^+} may be compared to the values estimated by Bernt et al.[18] for electrodes with the identical IrO_2/TiO_2 anode catalyst and loadings as a function of ionomer content: interpolating their data to an ionomer content of 8 wt.%, the authors estimated the anode R_{H^+} to range between 23–49 mΩcm$^2_{geo}$, which is consistent with the values shown in Fig. 8. Thus, by utilizing a Pt-WRE to determine the anode impedance spectra it was possible to extract the proton conduction resistance of the anode electrode in the cell. In previous works, the proton conduction resistance of the anode in a PEM-WE cell was determined from full-cell impedance spectra measured under blocking conditions that were established by purging the cathode with H_2 and the anode with N_2, assuming that the cathode does not contribute significantly to the full-cell impedance spectra.[32,36] That the latter assumption is correct under blocking conditions is shown by the comparably small magnitude of the cathode impedance compared to the anode impedance (see Figs. 7a and 7b). The use of the Pt-WRE, however, allows to deconvolute the ohmic resistance contributions from the anode and the cathode side of the MEA, clearly showing that the HFR only increases on the anode side. Possible unintended cationic contaminations of the ionomer phase in the membrane and the electrodes over the course of the OCV-AST can be excluded, as this would also have to lead to an increase of the cathode HFR, which clearly is not the case.

Besides the anode HFR and the anode proton conduction resistance, the use of the Pt-WRE also allows for an approximate quantification of the capacitance (C) of the anode electrode by fitting the TLM shown in Fig. 7a. While we use a constant phase element for the impedance fit, the α-value in all fits was always >0.9 so that the Q value of the constant phase element (in units of $F{\cdot}s^{(-1)}$) can be approximated with an actual capacitance (in units of F)). Figure 9b shows the development of the anode capacitance extracted from the anode impedance spectra acquired at a cell voltage of 1.3 V over the course of the OCV-AST. The anode capacitance of ≈318 mFcm$^{-2}_{geo}$ prior to the OCV-AST initially increases rather rapidly with the number of OCV-AST cycles, and then gradually levels off to a value of ≈505 mFcm$^{-2}_{geo}$ after 70 OCV-AST cycles. This increase of the anode capacitance clearly points towards a change of surface chemistry of the anode catalyst, consistent with the differences in the cyclic voltammetric features of the anode electrode (see Fig. 9a) when taken at the beginning-of-test (BoT, i.e., prior to the OCV-AST) and at the end-of-test (EoT, i.e., after 70 OCV-AST cycles). This shows that over the course of the OCV-AST, the originally crystalline IrO_2 phase of the IrO_2/TiO_2 anode catalyst with the typical CV observed at BoT (dark red CV in Fig. 9a) gradually converts into a hydrous iridium-oxide (light red CV in Fig. 10a) due to the exposure of the catalyst to hydrogen during the OCV periods.[29,30] The hydrous iridium-oxide exhibits the characteristic Ir(III)/Ir(IV) redox-features at ≈0.75 V,[37,38] and also has a significantly higher capacitance, e.g., ≈510 mFcm$^{-2}_{geo}$ at 1.0 V compared to ≈250 mFcm$^{-2}_{geo}$ for crystalline IrO_2 (see Fig. 9a). These findings are consistent with the irreversible transition of crystalline IrO_2 to a hydrous iridium-oxide observed in our previous OCV-AST study.[6] The capacitance values determined from the anode impedance spectra at 1.3 V (Fig. 9b) are in reasonably good agreement with those obtained by the CVs at 1.0 V (Fig. 9a). This confirms that the use of the Pt-WRE electrode indeed enables the determination of the anode capacitance from the anode impedance data.

In summary, the application of a Pt-WRE allows for the determination of the individual HFR as well as the anode proton conduction resistance of the anode and its capacitance under OCV conditions. During operation, however, the water distribution and content within the cell can change with current densities, as will the proton conduction resistance and the high frequency resistances of both anode and cathode. Moreover, the surface chemistry of the iridium might change at higher currents, which would lead to a concomitant change in capacitance. Hence, the values obtained at 1.3 V can be taken as indication for any changes observed over the course of the OCV-AST, but cannot be used to quantitatively capture individual performance loss contributions during operation.

Origin of the increasing HFR over the course of an OCV-AST.—The main cause for a decreasing performance during an OCV-AST was found to be an increasing HFR, which in principle can result either from a higher proton transport resistance of the membrane due to cationic contaminants and/or an additional electronic resistance. In this section, we will review and discuss the different reasons for an increasing HFR, which are illustrated in

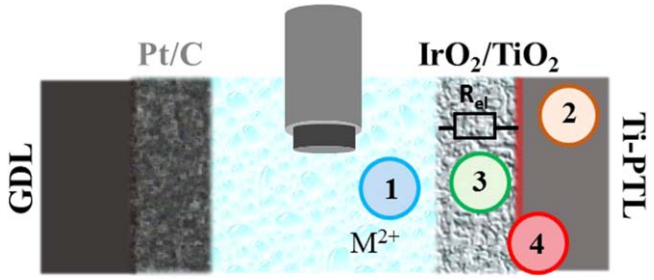

Figure 10. Scheme of an MEA with a Pt-WRE, illustrating possible reasons for the observed HFR increase during the OCV-AST: 1) cationic contamination of the membrane; 2) formation of an electronically insulating oxide film on the Ti-PTL surface; 3) additional resistance due to the low electronic conductivity of hydrous iridium-oxide; 4) additional interfacial resistance at the interface of the anode electrode and the titanium PTL due to passivation of Ti-PTL in combination with the lower electronic conductivity of the anode catalyst.

Fig. 10. One common failure mechanism for PEM water electrolyzers is a decreasing performance due to ion-exchanging the protons of the sulfuric acid groups of the ionomer membrane by cationic contaminants (① in Fig. 10), often introduced by insufficiently cleaned feed water.[39–42] Since the deionized (DI) feed water quality was recorded and monitored continuously over the course of the OCV-AST and since the resistivity of the feed water was always maintained at ⩾15 MΩcm, an introduction of cationic contaminants via the feed water was considered highly unlikely; alternatively, cationic contaminants could also result from the corrosion of cell hardware components, but post-mortem analysis of the membrane seemed to exclude also that possibility.[6] The observation in the present study that the cathode HFR ($HFR_{cathode}$, see Fig. 8) remains constant over the 70 OCV-AST cycles while the anode HFR (HFR_{anode}) and the full-cell HFR (HFR_{cell}) increase by the same rate now allows to unequivocally exclude any cationic contaminant effects: in case of cationic contamination, both sides of the membrane would be affected and, therefore, the $HFR_{cathode}$ would have to increase as well, especially since cations would be driven to the cathode side of the cell. The constant proton conduction resistance of the anode (red diamonds in Fig. 8) further proves that cationic contaminants are not the cause of the increasing full-cell HFR.

An increasing HFR due to the passivation of the Ti-PTL during operation and the accompanied increasing contact resistance at the anode (② in Fig. 10)[43] was already investigated in our previous OCV-AST study by contact resistance ($R_{cont.}$) measurements between the PTL and the flow field performed ex situ.[6,18] It was shown, that an increasing contact resistance indeed contributes to the increasing HFR, but this can only partially explain the overall increase. Moreover it is known that a hydrous iridium-oxide exhibits a lower electronic conductivity compared to crystalline IrO_2[7] and that if the electronic resistance of the catalyst layer is not significantly smaller than the ionic resistance (1/100) this would be reflected in the HFR.[44] Therefore, a decreasing electronic through-plane resistance of the catalyst layer might be responsible for the observed increase in HFR during cycling (③ in Fig. 10). The formation of a hydrous iridium-oxide was proven by both an increasing anode capacitance during cycling as well as by the formation of the typical Ir(III)/Ir(IV) redox features (Fig. 9). Additionally, in-plane resistance measurements showed that the electronic in-plane resistance of the IrO_2 is indeed lower at BoT ($\approx$0.04 $m\Omega cm^2_{geo}$) compared to the in-plane resistance determined at EoT upon the formation of a hydrous iridium-oxide ($\approx$0.08 $m\Omega cm^2_{geo}$).[6] Since this electronic resistance is still small compared to the ionic resistance, it would not lead to an increase of the full-cell or anode HFR. Hence, the only feasible explanation, as already concluded in the previous study,[6] is an interfacial resistance at the interface of the anode electrode and the Ti-PTL (④ in Fig. 10), due to a decreased electronic conductivity of the hydrous iridium-oxide catalyst layer in combination with the increased contact resistance due to the passivation of the Ti-PTL. Due to the coarse structure of the Ti-PTL (10–50 μm pores)[15] and the resulting small contact area between the Ti-PTL and anode electrode, even a small change in conductivity might lead to a significant increase in contact resistance.[6]

Conclusions

In this study a Pt wire micro-reference electrode (Pt-WRE) was applied in between the electrodes of a membrane electrode assembly (MEA) for a PEM water electrolyzer (PEM-WE) by laminating an insulated 50 μm Pt-wire between two 50 μm Nafion® membranes, with the aim to measure the individual electrode potentials and impedances. By comparing the performance of an MEA with the Pt-WRE to previous data recorded for an MEA without a Pt-WRE, it could be shown that the Pt-WRE does not affect MEA performance. Since the potential at the Pt-WRE depends on the ratio of the local permeation rates of O_2 and H_2 through the membrane, it changes with different operating pressures and current densities. However, for the applied anode and cathode pressures of 1.0 and 10 bar_a, the potential of the Pt-WRE is close to the reversible hydrogen potential (i.e., at $\approx$0 V_{RHE}) and can be used to determine the individual half-cell potentials of anode and cathode separately at low current densities (e.g., during OCV and potential holds at an electrolyzer voltage of 1.3 V). Even though it is not possible to obtain artefact-free anode or cathode impedance spectra while drawing significant electrolyzer currents due to the changing Pt-WRE potential, artefact-free electrode impedances can be obtained at OCV or at a 1.3 V potential hold

The Pt-WRE was used to study the degradation observed in our previously proposed OCV-AST, where periods of high and low current densities (3 Acm^{-2}_{geo} and 0.1 Acm^{-2}_{geo}) alternate with idle periods (OCV), mimicking electrolyzer operation with a fluctuating power supply. This allowed to prove that the anode potential drops close to the reversible hydrogen potential during the OCV-period, whereas the cathode potential remains at $\approx$0 V_{RHE}. Over the course of 70 OCV-AST cycles, the electrolyzer performance decreased by $\approx$10 mV at 3 Acm^{-2}_{geo}, which can be mostly ascribed to an increase in full-cell HFR ($\Delta HFR_{cell} \approx 5\ m\Omega cm^2_{geo}$).

The Pt-WRE was used to measure anode impedance spectra at an electrolyzer voltage of 1.3 V, where the charge transfer resistance of the OER is very large and the anode impedance can be described by a simplified transmission line model (TLM). During the OCV-AST, the cathode HFR (measured between the Pt-WRE and the cathode flow field) remained constant ($\approx$47 $m\Omega cm^2_{geo}$), whereas the full-cell HFR and the anode HFR (measured between the Pt-WRE and the anode flow field) both increased by $\approx$6 $m\Omega cm^2_{geo}$ over the course of 70 OCV-cycles. Thus the increasing full-cell HFR and the accompanied decrease in electrolyzer performance is related to an increasing HFR at the anode side. Since the cathode HFR and the anode proton conduction resistance remained constant over the course of the OCV-AST, an increase of the HFR due to cationic contaminants can be ruled out. Ultimately, the decreasing performance can be ascribed to an increasing contact resistance between the Ti-PTL in combination with a lower conductivity of the IrO_2-based anode catalyst due to the formation of a hydrous iridium-oxide during the OCV-periods. The formation of a hydrous iridium-oxide could be proven by both the increasing anode capacitance extracted from the anode impedance spectra via a transmission line model fit and by the development of the characteristic Ir(III)/Ir(IV) redox-features observed in the recorded CVs at the end-of-test.

In summary, the implementation of a Pt-WRE allows for a detailed electrode resolved impedance analysis of both anode and cathode, and thus enables the extraction of meaningful physical-chemical parameters such as anode and cathode HFR, the anode proton conduction resistance, and the anode capacitance.

Acknowledgments

This work was funded by the German Ministry of Education and Research (funding number 03SFK2V0, Kopernikus project P2X). We thank Dr. Johannes Landesfeind, Anna T.S. Freiberg, Dr. Daniel Pritzl, Robert Morasch, and Dr. Bharat Suthar for the fruitful and helpful scientific discussions.

ORCID

Alexandra Hartig-Weiß https://orcid.org/0000-0001-7094-5016
Maximilian Bernt https://orcid.org/0000-0001-8448-5532
Armin Siebel https://orcid.org/0000-0001-5773-3342
Hubert A. Gasteiger https://orcid.org/0000-0001-8199-8703

References

1. F. Barbir, "PEM electrolysis for production of hydrogen from renewable energy sources." *Sol. Energy*, **78**, 661 (2005).
2. A. Buttler and H. Spliethoff, "Current status of water electrolysis for energy storage, grid balancing and sector coupling via power-to-gas and power-to-liquids: a review." *Renew. Sustain. Energy Rev.*, **82**, 2440 (2017).
3. K. E. Ayers, E. B. Anderson, K. Dreier, and K. W. Harrison, "Fueling vehicles with sun and water." *ECS Trans.*, **50**, 35 (2013).
4. A. S. Aricò, S. Siracusano, N. Briguglio, V. Baglio, A. Di Blasi, and V. Antonucci, "Polymer electrolyte membrane water electrolysis: status of technologies and potential applications in combination with renewable power sources." *J. Appl. Electrochem.*, **43**, 107 (2013).
5. R. Clarke, S. Giddey, F. Ciacchi, S. Badwal, B. Paul, and J. Andrews, "Direct coupling of an electrolyser to a solar PV system for generating hydrogen." *Int. J. Hydrogen Energy*, **34**, 2531 (2009).
6. A. Weiß, A. Siebel, M. Bernt, T.-H. Shen, V. Tileli, and H. A. Gasteiger, "Impact of intermittent operation on lifetime and performance of a PEM water electrolyzer." *J. Electrochem. Soc.*, **166**, F487 (2019).
7. E. Rasten, G. Hagen, and R. Tunold, "Electrocatalysis in water electrolysis with solid polymer electrolyte." *Electrochim. Acta*, **48**, 3945 (2003).
8. S. Solchenbach, D. Pritzl, E. J. Y. Kong, J. Landesfeind, H. A. Gasteiger, and A. Gold, "Micro-reference electrode for impedance and potential measurements in lithium ion batteries." *J. Electrochem. Soc.*, **163**, A2265 (2016).
9. O. Sorsa, J. Nieminen, P. Kauranen, and T. Kallio, "Stable reference electrode in polymer electrolyte membrane electrolyser for three-electrode measurements." *J. Electrochem. Soc.*, **166**, F1326 (2019).
10. Z. Siroma, R. Kakitsubo, N. Fujiwara, T. Ioroi, S.-I. Yamazaki, and K. Yasuda, "Compact dynamic hydrogen electrode unit as a reference electrode for PEMFCs." *J. Power Sources*, **156**, 284 (2006).
11. G. Li and P. G. Pickup, "Measurement of single electrode potentials and impedances in hydrogen and direct methanol pem fuel cells." *Electrochim. Acta*, **49**, 4119 (2004).
12. S. B. Adler, "Reference electrode placement in thin solid electrolytes." *J. Electrochem. Soc.*, **149**, E166 (2002).
13. S. Adler, B. Henderson, M. Wilson, D. Taylor, and R. E. Richards, "Reference electrode placement and seals in electrochemical oxygen generators." *Solid State Ionics*, **134**, 35 (2000).
14. E. Brightman, J. Dodwell, N. van Dijk, and G. Hinds, "In situ characterisation of PEM water electrolysers using a novel reference electrode." *Electrochem. Commun.*, **52**, 1 (2015).
15. M. Bernt, A. Siebel, and H. A. Gasteiger, "Analysis of voltage losses in pem water electrolyzers with low platinum group metal loadings." *J. Electrochem. Soc.*, **165**, F305 (2018).
16. J. Landesfeind, D. Pritzl, and H. A. Gasteiger, "An analysis protocol for three-electrode li-ion battery impedance spectra: part I. analysis of a high-voltage positive electrode." *J. Electrochem. Soc.*, **164**, A1773 (2017).
17. D. Pritzl, J. Landesfeind, S. Solchenbach, and H. A. Gasteiger, "An analysis protocol for three-electrode li-ion battery impedance spectra: part II. analysis of a graphite anode cycled Vs Lnmo." *J. Electrochem. Soc.*, **165**, A2145 (2018).
18. M. Bernt and H. A. Gasteiger, "Influence of ionomer content in Iro2/Tio2 electrodes on PEM water electrolyzer performance." *J. Electrochem. Soc.*, **163**, F3179 (2016).
19. G. Inzelt, A. Lewenstam, and F. Scholz, *Handbook of Reference Electrodes* (Springer, Berlin) (2013).
20. M. Ender, A. Weber, and I.-T. Ellen, "Analysis of three-electrode setups for ac-impedance measurements on lithium-ion cells by FEM simulations." *J. Electrochem. Soc.*, **159**, A128 (2011).
21. S. Takaichi, H. Uchida, and M. Watanabe, "Distribution profile of hydrogen and oxygen permeating in polymer electrolyte membrane measured by mixed potential." *Electrochem. Commun.*, **9**, 1975 (2007).
22. W. Liu and D. Zuckerbrod, "In situ detection of hydrogen peroxide in PEM fuel cells." *J. Electrochem. Soc.*, **152**, A1165 (2005).
23. J. Zhang, B. A. Litteer, W. Gu, H. Liu, and H. A. Gasteiger, "Effect of hydrogen and oxygen partial pressure on Pt precipitation within the membrane of PEMFCs." *J. Electrochem. Soc.*, **154**, B1006 (2007).
24. M. Bernt, J. Schröter, M. Möckl, and H. Gasteiger, "Analysis of gas permeation phenomena in a PEM water electrolyzer operated at high pressure and high current density." *J. Electrochem. Soc.*, **167**, 124502 (2020).
25. P. Trinke, B. Bensmann, and R. Hanke-Rauschenbach, "Experimental evidence of increasing oxygen crossover with increasing current density during PEM water electrolysis." *Electrochem. Commun.*, **82**, 98 (2017).
26. A. Hartig-Weiß, *Current Challenges in Stability Assessment of Oxygen Evolution Reaction Catalysts for PEM Water Electrolyzer PhD Thesis (submitted)*, Technical University of Munich (2021).
27. P. J. Rheinländer, M. Bernt, Y. Incedag, and H. A. Gasteiger, "Stability and OER activity of IrO_x in PEM water electrolysis." *Meeting Abstracts*, **38**, 2427 (2016), MA-022016.
28. G. Papakonstantinou and K. Sundmacher, "H2 Permeation through N117 and Its consumption by IrO_x in PEM water electrolyzers." *Electrochem. Commun.*, **108**, 106578 (2019).
29. M. F. Tovini, A. M. Damjanovic, H. A. El-Sayed, J. Speder, C. Eickes, J.-P. Suchsland, A. Ghielmi, and H. Gasteiger, "Degradation mechanism of an IrO_2 anode co-catalyst for cell voltage reversal mitigation under transient operation conditions of a PEM fuel cell." *J. Electrochem. Soc.*, **168**, 064521 (2021).
30. P. J. Rheinländer and J. Durst, "Transformation of the oer-active IrO_x species under transient operation conditions in PEM water electrolysis." *J. Electrochem. Soc.*, **168**, 024511 (2021).
31. Y. Liu, M. W. Murphy, D. R. Baker, W. Gu, C. Ji, J. Jorne, and H. A. Gasteiger, "Proton conduction and oxygen reduction kinetics in pem fuel cell cathodes: effects of ionomer-to-carbon ratio and relative humidity." *J. Electrochem. Soc.*, **156**, B970 (2009).
32. U. Babic, E. Nilsson, A. Pătru, T. J. Schmidt, and L. Gubler, "Proton transport in catalyst layers of a polymer electrolyte water electrolyzer: effect of the anode catalyst loading." *J. Electrochem. Soc.*, **166**, F214 (2019).
33. R. Morasch, J. Landesfeind, B. Suthar, and H. A. Gasteiger, "Detection of binder gradients using impedance spectroscopy and their influence on the tortuosity of li-ion battery graphite electrodes." *J. Electrochem. Soc.*, **165**, A3459 (2018).
34. T. Reshetenko and A. Kulikovsky, "Impedance spectroscopy study of the PEM fuel cell cathode with nonuniform nafion loading." *J. Electrochem. Soc.*, **164**, E3016 (2017).
35. H. Kuhn, B. Andreaus, A. Wokaun, and G. Scherer, "Electrochemical impedance spectroscopy applied to polymer electrolyte fuel cells with a pseudo reference electrode arrangement." *Electrochim. Acta*, **51**, 1622 (2006).
36. U. Babic, T. J. Schmidt, and L. Gubler, "Communication—Contribution of catalyst layer proton transport resistance to voltage loss in polymer electrolyte water electrolyzers." *J. Electrochem. Soc.*, **165**, J3016 (2018).
37. S. Geiger, O. Kasian, B. R. Shrestha, A. M. Mingers, K. J. J. Mayrhofer, and S. Cherevko, "Activity and stability of electrochemically and thermally treated iridium for the oxygen evolution reaction." *J. Electrochem. Soc.*, **163**, F3132 (2016).
38. S. Ardizzone, A. Carugati, and S. Trasatti, "Properties of thermally prepared iridium dioxide electrodes." *J. Electroanal. Chem. Interfacial Electrochem.*, **126**, 287 (1981).
39. N. Danilovic, K. E. Ayers, C. Capuano, J. N. Renner, L. Wiles, and M. Pertoso, "(Plenary) challenges in going from laboratory to megawatt scale PEM electrolysis." *ECS Trans.*, **75**, 395 (2016).
40. S. A. Grigoriev, D. G. Bessarabov, and V. N. Fateev, "Degradation mechanisms of MEA characteristics during water electrolysis in solid polymer electrolyte cells." *Russ. J. Electrochem.*, **53**, 318 (2017).
41. U. Babic, M. Suermann, F. N. Büchi, L. Gubler, and T. J. Schmidt, "Critical review—identifying critical gaps for polymer electrolyte water electrolysis development." *J. Electrochem. Soc.*, **164**, F387 (2017).
42. S. Siracusano, N. Van Dijk, R. Backhouse, L. Merlo, V. Baglio, and A. Aricò, "Degradation issues of PEM electrolysis MEAs." *Renewable Energy*, **123**, 52 (2018).
43. C. Rakousky, U. Reimer, K. Wippermann, M. Carmo, W. Lueke, and D. Stolten, "An analysis of degradation phenomena in polymer electrolyte membrane water electrolysis." *J. Power Sources*, **326**, 120 (2016).
44. J. Landesfeind, M. Ebner, A. Eldiven, V. Wood, and H. A. Gasteiger, "Tortuosity of battery electrodes: validation of impedance-derived values and critical comparison with 3d tomography." *J. Electrochem. Soc.*, **165**, A469 (2018).